Effect of Magnetic Field on Partial Discharge Dynamics in Insulation Systems of Transportation Power Devices

Marek Florkowski, *Senior Member, IEEE*

***Abstract*— The globally observed trend toward electrically supplied devices is common in the transportation segment. Traditionally, the performance of electrical insulation has been assessed with respect to electric stresses and endurance. In all current-carrying devices, magnetic fields will also be superimposed on electric ones; therefore, the influence of a magnetic field's exposure on partial discharge (PD) dynamics is an actual research topic. This problem is important in the transportation segment as well, where low- and medium-voltage levels are mostly used for supply and energy conversion (which are associated with high load currents). This article is focused on the influence of magnetic fields on the dynamics of PDs in the voids of insulation systems of transportation power devices and refers to both ac and dc cases. A rather weak magnetic field (80 mT) was established in order to detect and analyze early stages of PD behavior. The measurements of PDs that were carried out in a dedicated setup revealed their impact on PD intensity, which have been visualized in time-sequence diagrams and PD images. This detected effect is attributed to both the elongation of the charged particle trajectory and the enhancement of the electron energy due to acceleration. It has been shown that the impact of a magnetic field can be observed within a supply voltage frequency range of 20–400 Hz (which is typical for the transportation segment). The PD intensity was amplified in the above range at a magnetic field induction of 80 mT (even up to 50%). The effect of a magnetic field can be recognized as an additional modulation factor that influences the dynamics of PDs.**

***Index Terms*— Electric transportation devices, electrical insulation, magnetic field, partial discharges (PDs).**

I. Introduction

THE global requirements of reducing CO_2 and NO_x (carbon dioxide and nitrogen oxides) emissions and switching to renewable energy sources bring electrical energy to the forefront of carriers. The globally observed trend toward electrically supplied devices is common in the transportation segment; this refers to all branches, starting with rail, marine, and electric vehicles (EVs) up to more-electric aircraft (MEA) and all-electric aircraft (AEA). Going even further, electrically driven elements are at the core of various planned space applications. In all of these applications (both ac and dc), electric and magnetic fields are present. Traditionally, the performance of electrical insulation has been assessed with respect to electric stresses and endurance. One of the crucial parameters of electric insulation is the presence and levels of partial discharges (PD). PDs reflect the condition and trend of electrical insulation integrity. In all current-carrying devices, magnetic fields will also be superimposed on electric ones; therefore, the influence of magnetic field exposure on partial discharge dynamics is an actual research topic. This problem is important in the transportation segment as well, where low- and medium-voltage (MV) levels are mostly used for supply and energy conversion (which are associated with high load currents). The ongoing development of power devices for the transportation segment is dominated by power electronics-based solutions; the key components are ac/dc and dc/dc converters. Storage applications will also require dc/ac inverters. A new class of applications will be related to power devices for hydrogen-based conversions. The trends toward higher electrical voltage levels in these applications are illustrated in Fig. 1. The above trend also triggers advanced research activities in the field of electrical insulation, seeking ultrareliable lightweight materials that allow for high-power density designs. The observed and natural evolution toward higher voltage levels will impose new requirements on electrical insulation systems.

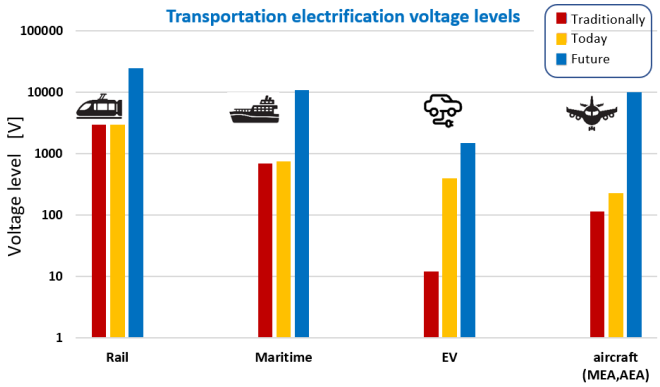

Fig. 1. Electric voltage levels in transportation segments: rail, maritime, EV, and aircraft.

These new challenges are related to the continuous operations under nonsinusoidal impulse conditions. In addition, high-frequency switching, ultrafast impulse rise and fall times (already in the nanosecond range, for example, in the case of wide bandgap semiconductors) [1], [2], and potential transients and overvoltages make these demands even more complex.

Manuscript received 17 March 2022; revised 7 June 2022; accepted 15 June 2022. Date of publication 23 June 2022; date of current version 21 October 2022.

The author is with the Electrical and Power Engineering Department, AGH University of Science and Technology, 30059 Kraków, Poland (e-mail: marek.florkowski@agh.edu.pl).

Digital Object Identifier 10.1109/TTE.2022.3185931

In order to reduce losses while increasing power, voltage levels are being shifted higher and higher in the transportation applications that cover the following segments: rail, EVs, more/all electric aircraft, marine, and hydrogen conversion.

There are various forms of discharges that are related to the defects that can be found inside or on the surface of electric insulation. One of the most common is a gaseous inclusion called a void. This PD development is associated with streamer stages such as inception, formation, and development. Streamers are usually elucidated as tiny channels of ionized gas and develop along electric field lines. In the presence of a magnetic field that is superimposed on an electric one, the streamer propagation trajectory is modified due to the additional Lorentz force that acts on the particles, which leads to a complex circular movement. The effect of an external magnetic field on the statistical parameters of PDs in inclusions was analyzed in [3] and [4]. Since PD images are the state-of-the-art in the HV insulation diagnostics of power equipment nowadays [5]–[17], the impact of adjacent factors such as background magnetic fields is crucial for the proper interpretation of any measurement results (similar to voltage harmonics) [18]. It was reported in [19] that stray leakage magnetic fields of up to 700 mT may be present in transformers (and even much higher fields can occur during short-circuit currents). The influence of a perpendicular magnetic field within a range of 350–550 mT on electrical treeing in cross-linked polyethylene (XLPE) cable insulation was investigated in [20]. The effect of a high-gradient magnetic field on tree growth in epoxy resin was shown in [21] and [22]. The experiments indicated that the electrical tree inception and development was easier in a gradient magnetic field. This effect was partly attributed to the increase of epoxy resin conductivity and dielectric loss tangents as well as the decrease of relative permittivity in the presence of a strong magnetic field. It was also reported that a magnetic field promoted the growth of electrical trees at low and cryogenic temperatures [23], [24]. The importance of this topic in the transportation segment can be highlighted with a few examples. Modern transportation devices deal with high electric power and high current applications that reach up to a few kA (especially in power electronics-driven solutions). This refers to the distribution grids of EVs, magnetic bearing drive systems, drives, generators, and motors. In the last one, the magnetic field induction in airgaps can even reach the Tesla level [25], [26]. The leakage flux in transformers (including high-frequency solid-state devices for traction or more electric aircraft applications) may reach up to hundreds of mT [27]. Such transformers for power electronics converters contain magnetic fluxes that penetrate their electrical insulation. A separate class refers to high-speed train solutions with magnetic levitation (where the magnetic induction is often above the Tesla level) [28]. There is ongoing research toward superconducting elements in the modern transportation sector (e.g., high-speed rail). Lightweight high-performance superconductors can make transportation propulsion systems more powerful. For example, there is currently ongoing research on high-temperature superconducting cables [23]. Due to the high currents, high magnetic fields will be present in the proximity of the conductors (inside their insulating materials).

This article is focused on the influence of magnetic fields on the dynamics of partial discharges in the voids of the insulation systems of transportation power devices within a frequency range of 20–400 Hz. The detected magnetic field-modulated PD intensity is a novel element that is quantitatively presented in time-sequence diagrams. In addition to electric stress, the magnetic-driven effect seems to be important for the reliability of the insulation systems of high-power transportation devices.

II. Insulation Systems of Transportation Devices

A strong development can be observed in the electric insulating materials for power devices in the transportation segment. This has been driven by those challenges that are related to extremely high reliability at both high and low temperatures as well as low-pressure endurance. The transportation electrification applications include some common sectors such as rail. Over the last decade, the observed boost in EVs (including heavy trucks and buses, maritime electrification up to more, and all electric aircraft, storage systems, and hydrogen-based conversions) has also contributed to this development. As shown in Fig. 1, the rise in voltage levels (i.e., operating electric field stresses) can be observed in all transportation segments. For example, a modern-day aircraft's voltage typically ranges from 115 to 230 V (ac) within a frequency span of 350–800 Hz (typically, 400 Hz) [1] and a dc bus of $+/-270$ V [29]. According to the predictions and trends, voltage levels may even reach 10 kV (see Fig. 1). The key ingredients of these systems refer to electric powertrain components, and the common denominator is the ubiquitous power electronics that are comprised of both semiconductors and passive designs. The observed trend also refers to lightweight solutions that are achievable by replacing magnetic designs with solid-state transformers (even with air insulation), for example [30].

The voltage level of a railway electrification traction system can reach 25 kV today and occurs in both ac and dc versions. This is highly dependent on traffic density, rail infrastructures, and grid properties. A train's catenary voltage ranges can be split into two groups: one below 3 kV (dc) for a medium-power supply with light rail, metro, and interurban services, and the other from 7.5 to 24 kV (dc) for high-power high-speed trains [31].

In marine transportation, integrated electric propulsion systems have become a more welcome and beneficial approach for reducing emissions due to their clear economic benefits in fuel savings [32]. In the power systems of maritime transports, the power distribution voltage is usually determined based on the total power generation and consumption of the unit. Typically, the power supply is based on a $400 \div 690$ V (ac) bus system, with trends toward dc bus systems of 750 V (dc) for smaller vessels and 1 kV (dc) for larger ones [32], [33]. In maritime applications, onboard dc grids are developed in the form of modular power system platforms that are comprised of modules of power sources; these may include variable-speed generators, energy-storage units, fuel cells, or auxiliary systems. Currently, a low-voltage dc system architecture is usually

adopted for ships that require less than 1 MW; larger ships that demand more than 10 MW need an MVDC architecture [34]. Therefore, the on-board voltage level for small ships, ferries, and short-sea vessels is around 1 kV, while a medium voltage is applied (above 3 kV) for larger ships (which still need diesel generators or liquefied natural gas (LNG) generators to be the main power sources). The largest cruise ships can even require up to 11 kV.

The dc bus voltage in electric and hybrid vehicles is currently of an order of 200–800 V (dc) at a power of up to 100 kW [2]. For EVs, the most commonly used voltage level is 400 V, but higher voltage levels of up to 800 V are being tested (e.g., in the design of Formula E race cars), and some vendors are equipping cars with this voltage system [35]. The strong push toward longer traveling ranges and the fast-charging capabilities will result in the elevation of the voltage levels of EVs. These higher voltage levels will also lead to a reduction of losses with a square of the voltage value. In addition, designs that are based on SiC (silicon carbide) and GaN (gallium nitride) will lead to a reduction of thermal losses. In contrast, high switching frequencies and ultrafast slew rates of and order of 100 kV/μs are stressing more electrical insulation [36]. These trends and directions impose further challenges on electrical insulation.

In the case of aircraft, there are many different voltages on which the electrical components operate (both with ac and dc). Mostly, the onboard systems use three-phase 115 V (ac) at 400 Hz and/or 28 V (dc). Some new units have incorporated three-phase 230-V (ac) electric power with variable frequencies within a range of 360–800 Hz and $\pm$270 V (dc) that is derived for powering auxiliary devices [2]. Nowadays, aircraft operates at voltages below 1 kV; however, higher voltage levels are being considered in new developments. For example, NASA has envisioned voltage levels of at least $6 \div 10$ kV for more electric aircraft [29], [37], [38]. The aviation and space industry is carefully analyzing these trends and standardizations due to the required safety and reliability aspects that are crucial in these applications. In future designs, central distribution systems are being envisioned as dc buses that are connected by inverters to motors and by rectifiers to source generators. In future MEAs, the electrical distribution systems that will be onboard the aircraft are forecast to be at power levels of $4 \div 40$ MVA [29], [39]. Increases in the system levels of transportation power devices will implicate greater insulation thicknesses and distances that are dimensioned according to the withstand levels. The new power supply aircraft architecture of MEAs is based on a remote power distribution that improves efficiency and reliability. The switching is based on solid-state devices and contactors [1]. The PD-free requirement refers to subcomponents such as power electronics modules that are based on IGBT or wide bandgap switches [40]. In this context, an important part of whole-system reliability is the cabling that is used in transportation electrification (including joint and connector screening effects) while also considering extreme applications with the impacts of reduced pressure and thermal dissipation (as are experienced in MEAs) [42]. In high powertrain solutions, superconducting busbars that are equipped with proper electrical void-free insulation and heat-transfer capabilities are being envisioned [42].

Due to the fast rise times and elevated voltage levels of transportation motors, for example, insulation systems require stronger withstand voltages; this refers both to enameled wire coatings and impregnation resins [47]. At high altitudes, an aircraft's operation results in exposure of electrical insulation (e.g., cabling, converters, motors, etc.) to lower air pressures and the potential inception of partial discharges at lower voltages. To avoid PD occurrence in MEA applications, the insulation design strategy of laminated busbars in high-density converters has been proposed [44].

A variety of converter topologies have been considered and developed depending on applications that stress various aspects such as high efficiency, high power and high voltage, lightweight, high-power density, low electromagnetic interference, low current ripples, and wide input voltage ranges [44]. A reduction of PD intensity may be also achieved by going toward a higher number of converter levels as a tradeoff with cost [45]. The new generation of wide bandgap semiconductors imposes the challenges for designing the electrical insulating systems of power converters. The dielectric losses may be significant in the case of MV converters that are operated at higher PWM modulated switching frequencies. For example, it was shown that the dielectric losses of a medium-frequency transformer with a dc/dc converter (25 kW, transformation 7 kV to 400 V, operated at 48 kHz) embedded in epoxy resin represent a significant share (i.e., up to 17% of the total transformer losses), suggesting the improvement of the silicone elastomer insulation [46]. The advanced development is also ongoing on the insulating material side toward higher withstand levels, long-term endurance, and lightweight solutions [30]. It is, therefore, essential to select and test the appropriate medium- and high-voltage insulating materials for these applications. These usually take the form of solid insulation, but hybrid forms are also possible in the form of gels, porous materials, pressboards, and foams. Manufacturing technologies, such as resin impregnation, potting, the coating of wirers and armatures, and the application of flexible laminates, are also of great importance for achieving partial discharge-free and resistant insulation. Taking reduced dielectric withstand at low pressure in air into account, industrial and automotive e-drive-motor power trains need additional testing, and improvements for corona-resistant capabilities (especially with respect to the wiring and winding) should be implemented and executed [47].

III. Magnetic Field Impact on Discharge Trajectory

Magnetic fields are present in the insulation systems of transportation power devices such as motors, generators, drives, transformers, and cables. PD current pulses result from those discharges that occur in a strong electric field by the release and transport of charge carriers in the form of streamers that propagate along the electric field lines inside defects [48]. The discharge path may be embedded inside a gaseous void in dielectric material or can also be influenced by dielectric-adjacent surfaces or barriers [49], [50]. The electrical stress

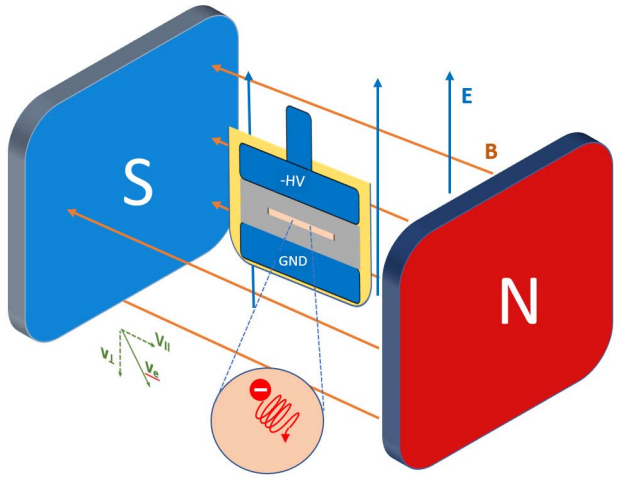

Fig. 2. Visualization of individual charge movement in crossed electric (E) and magnetic (B) fields.

is related to the applied voltage; however, the magnetic field depends on the load current. Thus, the current flow potentially introduces an additional factor that modulates the PD behavior. The dynamics and trajectories of the charges in gas that form a discharge profile are influenced by the magnetic field. The visualization of an individual charge movement that is an element of streamer formation in crossed electric and magnetic fields (E and B, respectively) is shown in Fig. 2.

The initial direction of charged particle velocity vector υ influences the drift trajectory (despite the orientation of the E and B fields). Along with the interaction of the electric and magnetic fields, the initial particle velocity shapes the trajectory along the helical, spiral, trochoidal, or cycloidal paths. The charge trajectory in gas is analyzed in this article without considering the surface and bulk effects in the dielectric material nor any collisions in air under a magnetic field at this stage. If the charge is moving in the presence of both the $\boldsymbol{E}$ and $\boldsymbol{B}$ fields, it will be affected by Lorentz force F_L

$$\boldsymbol{F}_L = q(\boldsymbol{E} + \mathbf{v} \times \boldsymbol{B}) \tag{1}$$

where q represents the particle charge, m is the particle mass, and υ is the particle velocity. The charged particle velocity vector shown in Fig. 2 has two components—perpendicular to, and parallel to the magnetic field vector. It is known that such a particle with a charge of q will execute a circular movement around the vector of magnetic field induction B with a frequency of f_B, which is inversely proportional to the particle mass

$$f_B = \frac{q}{2\pi m} B. \tag{2}$$

Assuming magnetic field induction $B = 100$ mT, for example, the corresponding frequency f_B is equal to 2.8 GHz in the case of electrons. In the electric field at accelerating voltage U, the electron transport velocity υ_e can be expressed as follows:

$$\upsilon_e = \sqrt{\frac{2eU}{m_e}} \tag{3}$$

where m_e is electron mass $9.1{\cdot}10^{-31}$ kg. The electron's circular trajectory radius r_e will be as follows:

$$r_e = \frac{\upsilon_e}{2\pi f_B}. \tag{4}$$

Assuming magnetic field $B = 100$ mT and accelerating voltage $U = 10$ kV, the radius of the electron cycling will be $r_e = 3.4$ mm.

Taking collision time τ into account, the particle drift equation in the crossed electric and magnetic fields yields [1]

$$m\frac{d\upsilon}{dt} = q(\boldsymbol{E} + \boldsymbol{\upsilon} \times \boldsymbol{B}) - \frac{m\upsilon}{\tau}. \tag{5}$$

Electron collision time τ can be expressed as follows:

$$\tau = \frac{\lambda_e}{\upsilon_e} = \lambda_e \sqrt{\frac{m_e}{kT_e}} \tag{6}$$

where λ_e denotes the electron mean free path, υ_e is the electron thermal velocity, k is Boltzmann's constant, and T_e is the electron temperature. The particles that propagate in the superimposed electric and magnetic fields undergo scattering, which can assume an elastic form (when the direction is changed but not the energy) or an inelastic form (for example, when an atom is ionized by a collision) [51]. The streamer path is determined by a trajectory that connects the successive ionization events. In this study, the electric field changed according to the applied voltage with a frequency of 50 Hz and the perpendicular magnetic field remaining constant. In fact, both fields can be treated as constant when analyzing the trajectories of the individual streamers since the discharge propagation time is within a range of nanoseconds.

IV. Simulation of Charged Particle Trajectory in Void in Crossed Electric and Magnetic Fields

The simulations were employed to analyze and visualize the trajectories of the charged particles in the coupled crossed electric and magnetic fields. The goal of the simulation was to analyze a hypothetical trajectory that was influenced by the superposition of both the electric and magnetic forces (excluding interactions of the particles, such as collisions). In a real environment, the streamer propagates due to the ongoing ionization process along the electric field lines. In this context, a crucial point is to analyze the impact on the path that resulted from the modification that was caused by the magnetic field. Since the individual streamer propagation time is within nanoseconds under real conditions, the simulated dc condition was assumed (corresponding to a tiny time slot on the sinusoidal waveform). The governing equation of the motion of a charged particle was solved with 3-D geometry in the presence of both fields. The simulations were executed in the COMSOL Multiphysics environment [52]. Actually, the simulation process is composed of two steps: in the first one, the electric and magnetic fields are calculated; and in the subsequent step, charge particle tracing is performed in these fields according to the motion equation with an applied superposition of electric and magnetic forces. In general, their trajectories can assume helical or cycloidal pathways in these fields; thus, 3-D simulations are recommended (especially

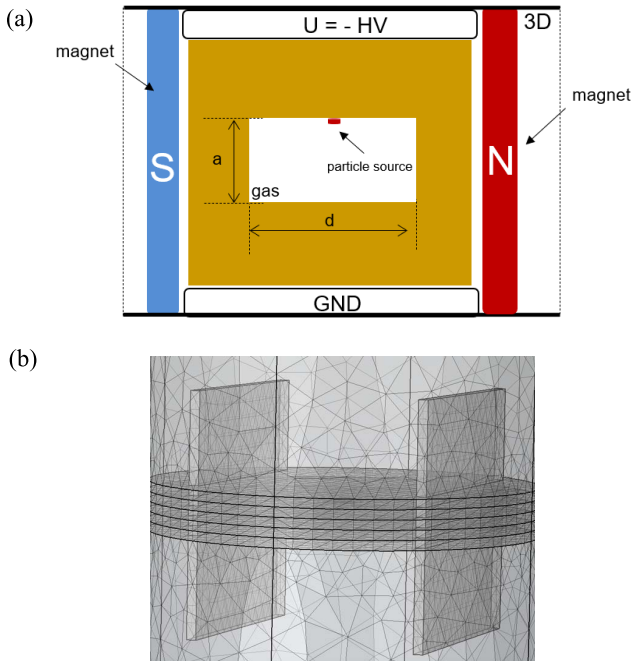

Fig. 3. Simulation model. (a) Cross section of 3-D configuration of simulation domain. (b) Visualization of the mesh.

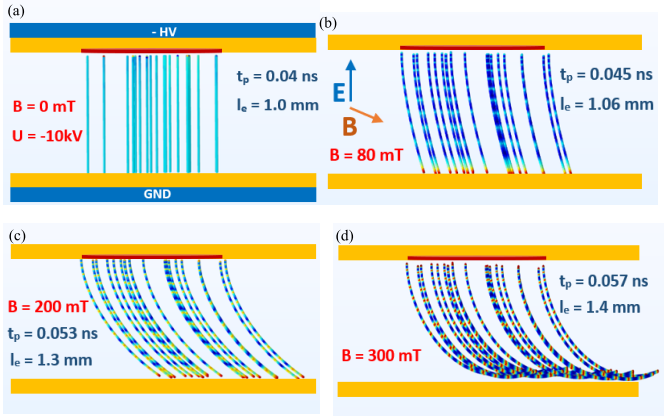

Fig. 4. Comparison of electron trajectories in embedded void ($a = 1$ mm, $d = 20$ mm) in crossed electric and magnetic fields at applied voltage $U = -10$ kV (−HV) for magnetic field induction: (a) $B = 0$ mT, (b) $B = 80$ mT, (c) $B = 200$ mT, and (d) $B = 300$ mT. Electrode description in Graph a, and orientation of E, B fields in Graph b; source of particles marked by red bar.

TABLE I
ELECTRON PROPAGATION TIME t_p AND TRAJECTORY LENGTH l_e IN VOID IN $E \times B$

	Magnetic field B [mT]			
	0	80	200	300
t_p [ns]	0.040	0.045	0.053	0.057
l_e [mm]	1.00	1.06	1.30	1.40

when magnetic or electric field nonuniformities or gradients along the axes are also considered). A cross section of the 3-D-model geometry of a gaseous inclusion is presented in Fig. 3. The dielectric material was polyethylene with a relative permittivity of 2.2. The meshing was based on tetrahedral elements [see Fig. 3(b)]. The HV and ground electrodes are placed on the top and bottom sides of the void. A source of particles that mimics the discharge origin and ionization zone is depicted by a tiny cone with a diameter of 1 mm on an upper void wall, releasing 20 particles in a sequence. In fact, this is a certain simplification that does not reflect those streamers that originate from the ionization in the airgap; however, it seems to be a good approximation for the intent of these simulations.

The simulations were based on the electron-tracing comparison. A mean kinetic energy of 100 eV with the Gaussian distribution with standard deviation σ being equal to 20 eV was defined as the initial condition for the electrons. For the graphical visualization, the particle trajectory was rendered as a tube. The simulations were carried out for a void thickness $a = 1$ mm and a diameter of $d = 20$ mm.

The following boundary conditions (indicated in Fig. 3) were assumed: the high-voltage potential was placed on the top electrode, and the bottom electrode was grounded. In the case when a particle touches a wall, the freeze option was assumed. The presented simulations were performed with dc voltage at a high-voltage electrode that was equal to −10 kV. The environmental conditions adhere to a standard case (STP); i.e., a temperature of 300 K, and a pressure of 0.1 MPa. Comparisons of the trajectories at an applied voltage of $U = -10$ kV are shown in Fig. 4 for the magnetic field-free case as well as for those scenarios with magnetic inductions B that were equal to 80, 200, and 300 mT. Without the magnetic field [$B = 0$ mT—Fig. 4(a)], the electrons moved along straight lines that followed the electric field lines from the beam source. Applying a perpendicular magnetic field caused the twisting and deflection of the trajectories [see Fig. 4(b) and (d)] according to the action and direction of the Lorentz force. Amplifying the magnetic field induction from 80 to 300 mT resulted in a circling of the beam around the magnetic field axis, with a simultaneous drift due to an electric field toward the grounded side of the void. Also notable are the impact of the magnetic field on charged particle propagation time t_p (also called the residence time) and the length of trajectory l_e. For a 1-mm-thick void, the electrons crossed the inclusion in the field-free situation within 0.04 ns, whereas the presence of magnetic fields with $B = 80$ mT, $B = 200$ mT, and $B = 300$ mT yielded 0.045, 0.053, and 0.057 ns, respectively, for time t_p.

Particle trajectory length l_e was elongated from an initial length of 1 mm (void thickness) in the field-free case to 1.06, 1.3, and 1.4 mm for magnetic field inductions $B = 80$ mT, $B = 200$ mT, and $B = 300$ mT, respectively. A comparison of these values is shown in Table I. It was observed that the longer moving path that was caused by the magnetic field deflection resulted in a longer residence and propagation time t_p of the whole trajectory inside the gaseous inclusion.

The presence of a magnetic field led to a more compact beam [e.g., Fig. 4(c) and (d)] that was not dispersed as it was in the field-free case [see Fig. 4(a)]. The evolution of the propagation trajectory over time for induction $B = 0.2$ T and voltage $U = -10$ kV is illustrated in Fig. 5.

The deflection of the trajectory can be observed in Fig. 5(b), which leads to a swirl [see Fig. 5(e)]—unless the electrons

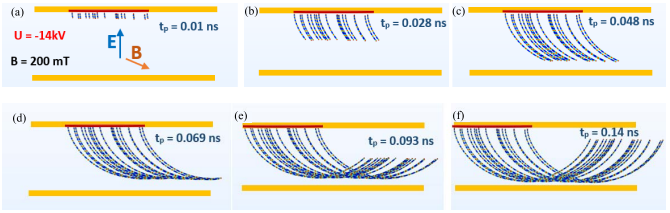

Fig. 5. Frame sequence of propagation trajectory development in embedded void over time for induction $B = 0.2$ T, $U = -10$ kV at the following time stamps: (a) 0.01 ns, (b) 0.028 ns, (c) 0.048 ns, (d) 0.069 ns, (e) 0.093 ns, and (f) 0.14 ns—orientation of E, B fields in Graph a; electrode setup as in Fig. 4(a).

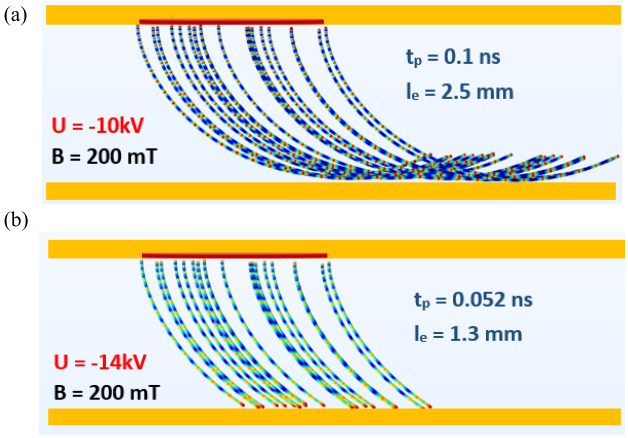

Fig. 6. Electron beam trajectories in crossed electric and magnetic fields in embedded void in magnetic field $B = 0.2$ T for applied voltages: (a) -10 kV and (b) -14 kV. Electrode description and orientation of E, B fields are the same as in Fig. 4.

reach the ground side void wall. In this way at certain ratios of the electric and magnetic forces and electron initial conditions, such an effect may lead to the attenuation (or even the stoppage) of the development of the discharges. The acceleration voltage (thus, the electric field strength) that was responsible for the particle transport influenced the shape of the charged particle trajectory.

This dependence of electrons in a magnetic field with $B = 0.2$ T in an embedded void arrangement is illustrated in Fig. 6 for the applied voltages of -10 and -14 kV. The residence time and particle trajectory length yielded in these cases were $t_p = 0.1$ ns/$l_e = 2.5$ mm and $t_p = 0.052$ ns/l_e= 1.3 mm, respectively. The increased voltage from -10 to -14 kV [see Fig. 6(b)] resulted in vertical transport acceleration along electric field vector E and the attenuation of the twisting effect caused by the magnetic field component. The aim of the simulations was to compare the beam trajectory modulation by a perpendicular magnetic field along with quantifications of the trajectory length and propagation time with respect to the magnetic field induction and applied voltage.

V. Experimental Setup and Instrumentation

The experiments on the influence of the magnetic field were carried out in the setup that is presented in Fig. 7. Since all of the elements of the experimental arrangement are exposed to the magnetic field, they should be made of a nonmagnetic material; this refers especially to the electrodes and connections. The high voltage and ground electrodes

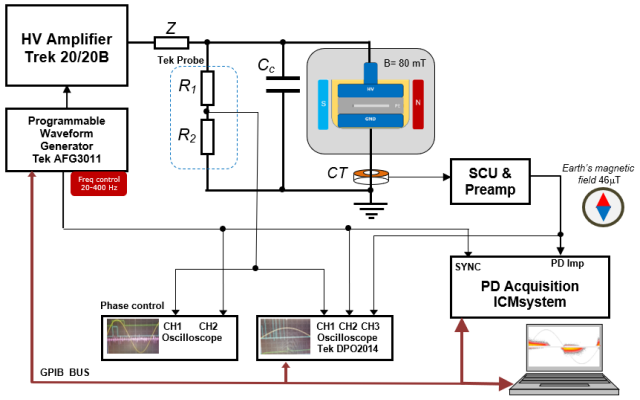

Fig. 7. Measurement setup for detection of partial discharges in embedded void in crossed electric and magnetic fields.

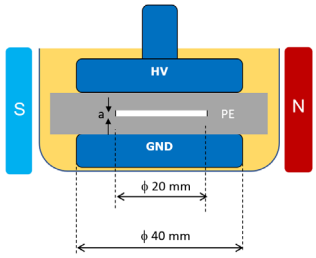

Fig. 8. Geometry of PE specimen containing embedded void.

(both made of polished aluminum) had a diameter of 40 mm. In order to prevent surface discharges, the setup with a specimen was immersed in oil in a plastic tub. Two permanent neodymium magnets that were located on both sides of the electrodes at a distance 70 mm created the quasi-uniform static magnetic field in this setup. The measured magnetic induction in the middle of the gap was 80 mT. The applied field is three orders of magnitude higher than Earth's magnetic field (e.g., in Krakow, this is $B_{\text{Earth}} = 46$ μT).

The investigations were performed in a specimen that contained a gaseous void that was embedded in dielectric material. As a representation of polymeric electrical insulation, polyethylene (PE) was used. The specimen was manufactured from the PE layers, with punched hole in a middle one to form the void. The sample geometry is presented in Fig. 8. The PE specimen had dimensions of 50 × 50 mm and a thickness of 3 mm. The internal void had a diameter of 20 mm and a thickness $a = 1$ mm. The electric permeability of the PE material was $\varepsilon_r = 2.2$.

The instrumentation contained a programmable high-voltage source, a control, and a PD-detection system. The HVAC sinusoidal waveform was supplied from an amplifier (Trek 20/20B) that was controlled by a function generator (Tektronix Model AFG 3011) for frequency adjustment. The coupling capacitor C_c that was placed in a parallel branch of the tested object closed the high-frequency PD loop. The PDs were detected using a wideband current transformer CT that was terminated at 50 Ω. The partial discharges were recorded in the wideband phase-resolved mode (PRPD) by means of Power Diagnostix's ICM-acquisition system, which was connected to a control unit through a GPIB bus.

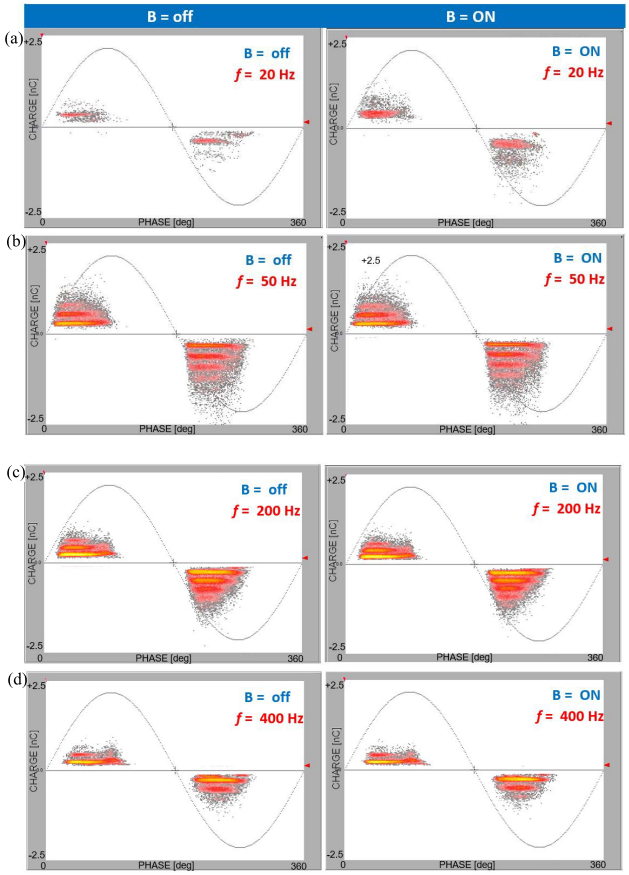

Fig. 9. PD patterns acquired at 10 kV for specimen that contained embedded voids without (left column) and with (right column) magnetic field presence at the following frequencies of high voltage: (a) 20 Hz, (b) 50 Hz, (c) 200 Hz, and (d) 400 Hz.

VI. Results and Discussion

The influence of a magnetic field on partial discharge dynamics was evaluated in the dedicated setup, which allowed us to obtain the required sensitivity. The measurements were performed especially in a relatively low-level magnetic field environment ($B = 80$ mT) in order to reflect the exposure conditions of real insulating systems. Since transportation power supply devices operate in a broad frequency range, the measurement was carried out from 20 to 400 Hz. The frequency dependence of the PD intensity is presented. The PD acquisition time in all of the PD sequences was 300 s. The PD inception voltage U_0 for these specimens was 8 kV (measured at 50 Hz). The PD phase-resolved patterns that were recorded at 10 kV for all of the frequencies are shown in Fig. 9. The shape revealed typical patterns for floating inclusions; i.e., not sticking to the electrode [7]. The recorded PD patterns without and with the magnetic field are quite similar except for the low-frequency case at 20 Hz, where one can recognize the clear intensity of the amplification that was caused by the presence of the magnetic field. In other cases, the magnetic field impact was mainly embedded in the intensity rather than in the spread of the charge magnitude. In order to notice the influence of the magnetic field, the measurements were executed in the time-sequence diagrams that indicated the stages with the magnetic field turned off ($B = \text{OFF}$) and on ($B = \text{ON}$).

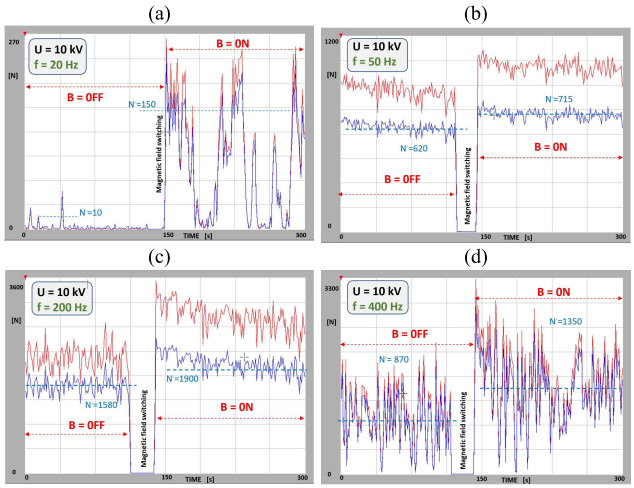

Fig. 10. Time-sequence PD diagrams ($B = \text{OFF}/B = \text{ON}$) of influence of magnetic field on PD intensity in polymeric specimen containing void at 10 kV with the following voltage frequencies: (a) 20 Hz, (b) 50 Hz, (c) 200 Hz, and (d) 400 Hz.

The time-sequence diagrams that corresponded to the measurements that were performed at frequencies within a range of 20–400 Hz are shown in Fig. 10. The two traces that are marked in the plot represent the numbers of positive and negative PD pulses (marked in red and blue, respectively). Intensity number N is related to the acquisition period of 300 s. As shown in all of the graphs in Fig. 10, switching the magnetic field ON resulted in a waveform sequence jump to the elevated level in the PD time recording of the B = OFF/ON sequence. For a frequency of 20 Hz at 10 kV in the magnetic field-free case, the PD intensity is very low; however, the PD intensity grew rapidly after turning on a magnetic field with an induction of 80 mT [as illustrated in the PD time sequence in Fig. 10(a)]. The amplification of the PD intensity after turning on the magnetic field may be attributed to the influence on the streamer trajectory. The elongated paths that were caused by the magnetic field caused circulations, which also increased the probability for ionization (and, thus, the occurrence and inception of discharges). In that context, it is important to mention that magnetic field is influencing the PD inception voltage.

The trajectories of both the electrons and ions were influenced by the coexistence of the electric and magnetic fields. The number of PD pulses of both polarities was at the same level throughout the sequence (at an average of ten pulses per record in the field-free part, increasing to 150 pulses after the magnetic field transition). At a higher voltage frequency of 50 Hz, the amplification of the negative number pulses averaged between 620 and 715 pulses; at 200 Hz, the number of pulses averaged between 1580 and 1900. A certain asymmetry could also be observed with respect to the polarity between the intensities of the negative and positive pulses. At a frequency of 400 Hz, a high discharge variation in the studied state without and with a magnetic field could be observed; more importantly, an elevation of the PD intensity was also noticed. Thus, the impact of the magnetic field on the PD intensity could be observed within the investigated frequency range of 20–400 Hz. The PD measurement that was carried out on the

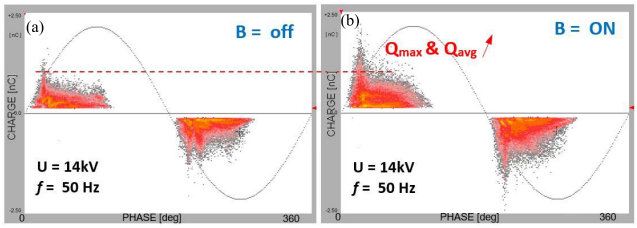

Fig. 11. PD patterns acquired at 14 kV ($1.7U_0$) at frequency of 50 Hz for specimen that contained embedded void. (a) Magnetic field-free. (b) With presence of magnetic field.

same specimen that contained an embedded void (at 14 kV, corresponding to a $1.7U_0$ inception voltage, and at a frequency of 50 Hz) revealed the magnetic field effect that is shown in the PD images in Fig. 11. Comparing the magnetic field-free scenario [see Fig. 11(a)] with a presence of a magnetic field with an induction of $B = 80$ mT [see Fig. 11(b)], one can notice the amplified discharge intensity as well as the increased maximal $Q_{\max}$ and average Q_{avg} charge levels. Since the flight paths of the charged particles (i.e., the electrons and ions) were modulated by the magnetic field, one can imagine that the geometry and dimensions of the defects will impact the final trajectories.

The effect that was shown in the embedded void would be also present in the case of surface or corona discharges (where longer interelectrode distances usually occur). The root causes of the observed phenomena were related to the magnetic field's enhanced number of collisions among the gas molecules, ions, and electrons along with the trajectory elongation and electron energy amplification by the magnetic field acceleration. An interesting observation that is reported in this article refers to the modulation of the PD intensity by the superimposed magnetic field.

VII. Conclusion

A clear trend can be observed in the elevation of the voltage levels of power devices in the transportation segment; this will result in higher electrical stresses on their insulation systems. In the cases of all current-carrying devices, their electrical insulation systems are also exposed to magnetic fields. The measurement methodology allowed us to detect magnetic field-modulated PD dynamics at low level of magnetic induction. With stronger magnetic fields, this effect will become more predominant and may result in the amplification (or under certain conditions and in certain configurations) of the attenuation of discharges. The measurements of partial discharges that were carried out in a dedicated setup revealed their impact on PD intensity, which has been visualized in time-sequence diagrams and PD images. The measurements revealed enhanced PD intensity in the presence of a magnetic field that can be observed in a supply voltage frequency range of 20–400 Hz (which is typical for the transportation segment). The PD intensity was amplified in the above range at magnetic field induction 80 mT, even up to 50%. This detected effect can be attributed to both the elongation of the charged particle trajectories and the enhancement of the electron energy due to particle acceleration. The effect of a magnetic field can be recognized as an additional factor that influences the dynamics of partial discharges. These simulations showed the deflections and elongations of the electrons' pathways (due to the effective Lorentz force), with a longer residence time benchmarking the magnetic field-free case. This effect can increase the probability of ionization, thus effectively increasing the discharge intensity. Any future research directions may evaluate the impact of magnetic fields on PD inception levels, various geometries of voids, and space-oriented magnetic field gradients.

The goal of the study was to contribute to the understanding of the physical phenomena and raise the awareness of PD-intensity modulation that is caused by the presence of magnetic fields in the electrical insulation of transportation electric power devices.

Acknowledgment

The author would like to thank Eng. Kazimierz Chudyba for his help with the magnetic setup arrangement.

References

[1] B. Sarlioglu and C. T. Morris, "More electric aircraft: Review, challenges, and opportunities for commercial transport aircraft," *IEEE Trans. Transport. Electrific.*, vol. 1, no. 1, pp. 54–64, Jun. 2015.

[2] K. Rajashekara, "Power conversion technologies for automotive and aircraft systems," *IEEE Electrific. Mag.*, vol. 6, pp. 50–60, Jun. 2014.

[3] A. J. Reid, D. M. Hepburn, and B. G. Stewart, "The influence of external magnetic fields on the partial discharge characteristics of voids," in *Proc. IEEE Electr. Insul. Conf. (EIC)*, Jun. 2013, pp. 147–150.

[4] S. K. Amizhtan, A. J. Amalanathan, R. Sarathi, H. Edin, and N. Taylor, "Impact of magnetic field on corona discharge behavior of mineral oil under AC voltage," *IEEE Trans. Electr. Insul.*, vol. 29, pp. 1–8, 2022, doi: 10.1109/TDEI.2022.3171737.

[5] B. Fruth and L. Niemeyer, "The importance of statistical characteristics of partial discharge data," *IEEE Trans. Electr. Insul.*, vol. 27, no. 1, pp. 60–69, Feb. 1992.

[6] C. Pan, G. Chen, J. Tang, and K. Wu, "Numerical modeling of partial discharges in a solid dielectric-bounded cavity: A review," *IEEE Trans. Dielectr. Electr. Insul.*, vol. 26, no. 3, pp. 981–1000, Jun. 2019.

[7] M. Florkowski, *Partial Discharges in High-Voltage Insulating Systems—Mechanisms, Processing, and Analytics*. Kraków, Poland: AGH Press, 2020.

[8] H. A. Illias, G. Chen, and P. L. Lewin, "Comparison between three-capacitance, analytical-based and finite element analysis partial discharge models in condition monitoring," *IEEE Trans. Dielectr. Electr. Insul.*, vol. 24, no. 1, pp. 99–109, Feb. 2017.

[9] G. Callender and P. L. Lewin, "Modeling partial discharge phenomena," *IEEE Elect. Insul. Mag.*, vol. 36, no. 2, pp. 29–36, Mar. 2020.

[10] M. Florkowski, "Autonomous tracking of partial discharge pattern evolution based on optical flow," *Measurement*, vol. 179, Jul. 2021, Art. no. 109513.

[11] V. Brunt, R. J. Kulkarni, and S. V., "Method for measuring the stochastic properties of corona and partial-discharge pulses," *Rev. Sci. Instrum.*, vol. 60, pp. 3012–3023, Sep. 1989.

[12] M. Florkowski, B. Florkowska, M. Kuniewski, and P. Zydron, "Mapping of discharge channels in void creating effective partial discharge area," *IEEE Trans. Dielectr. Electr. Insul.*, vol. 25, no. 6, pp. 2220–2228, Dec. 2018.

[13] T. Hammarstrom and S. M. Gubanski, "Detection of electrical tree formation in XLPE insulation through applying disturbed DC waveforms," *IEEE Trans. Dielectr. Electr. Insul.*, vol. 28, no. 5, pp. 1669–1676, Oct. 2021.

[14] H. Illias, G. Chen, and P. L. Lewin, "Partial discharge behavior within a spherical cavity in a solid dielectric material as a function of frequency and amplitude of the applied voltage," *IEEE Trans. Dielectr. Electr. Insul.*, vol. 18, no. 2, pp. 432–443, Apr. 2011.

[15] N. M. K. Abdel-Gawad, D.-E.-A. Mansour, A. Z. El Dein, H. M. Ahmed, and M. M. F. Darwish, "Effect of functionalized TiO_2 nanoparticles on dielectric properties of PVC nanocomposites used in electrical insulating cables," in *Proc. 18th Int. Middle East Power Syst. Conf. (MEPCON)*, Dec. 2016, pp. 693–698.

[16] N. M. K. Abdel-Gawad, A. Z. El Dein, D.-E.-A. Mansour, H. M. Ahmed, M. M. F. Darwish, and M. Lehtonen, "Experimental measurements of partial discharge activity within LDPE/TiO_2 nanocomposites," in *Proc. 19th Int. Middle East Power Syst. Conf. (MEPCON)*, Dec. 2017, pp. 811–816.

[17] N. M. K. Abdel-Gawad, D.-E.-A. Mansour, M. M. F. Darwish, A. Z. E. Dein, H. M. Ahmed, and M. Lehtonen, "Impact of nanoparticles functionalization on partial discharge activity within PVC/SiO_2 nanocomposites," in *Proc. IEEE 2nd Int. Conf. Dielectr. (ICD)*, Jul. 2018, pp. 1–4.

[18] M. Florkowski, M. Kuniewski, and P. Zydro, "Partial discharges in HVDC insulation with superimposed AC harmonics," *IEEE Trans. Dielectr. Electr. Insul.*, vol. 27, no. 6, pp. 1875–1882, Dec. 2020.

[19] J. M. Martínez-Tarifa, J. Rivas-Conde, G. Robles, and J. Sanz-Feito, "Influence of leakage magnetic fields on partial discharge activity in power transformers," *IEEE Trans. Dielectr. Electr. Insul.*, vol. 17, no. 6, pp. 1724–1730, Dec. 2010.

[20] Y. Gao, B. X. Du, and Z. L. Ma, "Effect of magnetic field on electrical treeing behavior in XLPE cable insulation," in *Proc. Int. Symp. Electr. Insulating Mater.*, Sep. 2011, pp. 457–461.

[21] M. Y. Wang, B. X. Du, X. X. Kong, Z. L. Li, M. Xiao, and Y. W. Ma, "Effects of gradient magnetic field on charge behavior and electrical tree growth in epoxy resin," *IEEE Trans. Dielectr. Electr. Insul.*, vol. 28, no. 5, pp. 1686–1693, Oct. 2021.

[22] M. Y. Wang, B. X. Du, X. T. Han, J. Li, Z. L. Li, and Y. Q. Xing, "Electrical treeing characteristics in epoxy under electromagnertic coupled field," in *Proc. 14th Eur. Conf. Appl. Supercond. (EUCAS)*, 2019, pp. 1–12.

[23] Y. Yu, B. X. Du, J. X. Jin, T. Han, and J. G. Su, "Effect of magnetic field on electrical treeing behavior of silicone rubber at low temperature," *IEEE Trans. Appl. Supercond.*, vol. 26, no. 7, pp. 1–4, Aug. 2016.

[24] B. X. Du, J. G. Su, and T. Han, "Effects of magnetic field on electrical tree growth in silicone rubber under repetitive pulse voltage," *IEEE Trans. Dielectr. Electr. Insul.*, vol. 22, no. 4, pp. 1785–1792, Aug. 2015.

[25] A. Barzkar and M. Ghassemi, "Components of electrical power systems in more and all-electric aircraft: A review," *IEEE Trans. Transport. Electrific.*, early access, May 11, 2022, doi: 10.1109/TTE.2022.3174362.

[26] S. Ding, W. Han, J. Sun, F. Jiang, G. Deng, and Y. Shi, "Modeling and analysis of a linear generator for high speed maglev train," *IEEE Access*, vol. 9, pp. 24637–24645, 2021.

[27] M. Eslamian, M. Kharezy, and T. Thiringer, "An accurate method for leakage inductance calculation of shell-type multi core-segment transformers with circular windings," *IEEE Access*, vol. 9, pp. 111417–111431, 2021.

[28] X. Li, W. Xu, K. Liao, and X. Wu, "Design of stator-magnet moving-iron transverse-flux linear oscillatory machine considering asymmetric saturation," *IEEE Trans. Transport. Electrific.*, early access, Feb. 18, 2022, doi: 10.1109/TTE.2022.3152909.

[29] R. Lowndes and I. Cotton, "Forecasting the partial discharge inception voltage (PDIV) of insulated busbars for future aircraft power distribution systems," in *Proc. IEEE Electr. Insul. Conf. (EIC)*, Jun. 2021, pp. 189–192.

[30] P. Czyz, T. Guillod, F. Krismer, J. Huber, and J. W. Kolar, "Design and experimental analysis of 166 kW medium-voltage medium-frequency air-core transformer for 1:1-DCX applications," *IEEE J. Emerg. Sel. Topics Power Electron.*, early access, Feb. 19, 2021, doi: 10.1109/JESTPE.2021.3060506.

[31] P. Cheng, H. Kong, J. Ma, and L. Jia, "Overview of resilient traction power supply systems in railways with interconnected microgrid," *CSEE J. Power Energy Syst.*, vol. 7, no. 5, pp. 1122–1132, 2021.

[32] G. Chang, Y. Wu, S. Shao, Z. Huang, and T. Long, "DC bus systems for electrical ships," *Electrific. Mag.*, vol. 9, pp. 28–39, Sep. 2020.

[33] A. Haxhiu, A. Abdelhakim, S. Kanerva, and J. Bogen, "Electric power integration schemes of the hybrid fuel cells and batteries-fed marine vessels—An overview," *IEEE Trans. Transport. Electrific.*, vol. 8, no. 2, pp. 1–21, Jun. 2021, doi: 10.1109/TTE.2021.3126100.

[34] L. Xu *et al.*, "A review of DC shipboard microgrids—Part II: Control architectures, stability analysis, and protection schemes," *IEEE Trans. Power Electron.*, vol. 37, no. 4, pp. 4105–4120, Apr. 2022.

[35] (2022). *Formula-E*. [Online]. Available: https://www.fiaformulae.com/

[36] D. E. Moghadam, C. Herold, and R. Zbinden, "Electrical insulation at 800 V electric vehicles," in *Proc. Int. Symp. Elect. Insulating Mater. (ISEIM)*, Sep. 2020, pp. 115–119.

[37] D. E. Moghadam, C. Herold, and R. Zbinden, "Effects of resins on partial discharge activity and lifetime of insulation systems used in eDrive motors and automotive industries," in *Proc. IEEE Electr. Insul. Conf. (EIC)*, Jun. 2020, pp. 221–224.

[38] M. Borghei and M. Ghassemi, "Classification of partial discharge in electric aircraft based on short-term behavior of insulation systems," in *Proc. AIAA Propuls. Energy Forum*, Aug. 2021, pp. 1–10.

[39] A. H. Epstein and S. M. O'Flarity, "Considerations for reducing aviation's CO_2 with aircraft electric propulsion," *J. Propuls. Power*, vol. 35, no. 3, pp. 572–582, May 2019.

[40] T. Shahsavarian, D. Zhang, P. McGinnis, S. Walker, Z. Zhang, and Y. Cao, "Altitude readiness of high-voltage IGBTs subjected to the partial discharge at harsh environmental conditions for hybrid electric aircraft propulsion," *IEEE Trans. Power Electron.*, vol. 37, no. 4, pp. 3733–3736, Apr. 2022.

[41] H. Xu, R. Lowndes, and I. Cotton, "Power capacity of high voltage cables for future electrical aircraft," in *Proc. IEEE Electr. Insul. Conf. (EIC)*, Jun. 2021, pp. 177–180.

[42] M. Yazdani-Asrami, S. M. Seyyedbarzegar, M. Zhang, and W. Yuan, "Insulation materials and systems for superconducting powertrain devices in future cryo-electrified aircraft: Part I-material challenges and specifications, and device-level application," *IEEE Elect. Insul. Mag.*, vol. 38, no. 2, pp. 25–36, Feb. 2022.

[43] Z. Yuan *et al.*, "Insulation and switching performance optimization for partial-discharge-free laminated busbar in more-electric aircraft applications," *IEEE Trans. Power Electron.*, vol. 37, no. 6, pp. 6831–6843, Dec. 2022.

[44] J. Chen, M.-K. Nguyen, Z. Yao, C. Wang, L. Gao, and G. Hu, "DC-DC converters for transportation electrification: Topologies, control, and future challenges," *IEEE Electrific. Mag.*, vol. 9, no. 2, pp. 10–22, Jun. 2021.

[45] M. Florkowski, P. Błaszczyk, and P. Klimczak, "Partial discharges in twisted-pair magnet wires subject to multilevel PWM pulses," *IEEE Trans. Dielectr. Electr. Insul.*, vol. 24, no. 4, pp. 2203–2210, Sep. 2017.

[46] T. Guillod, R. Faerber, D. Rothmund, F. Krismer, C. M. Franck, and J. W. Kolar, "Dielectric losses in dry-type insulation of medium-voltage power electronic converters," *IEEE J. Emerg. Sel. Topics Power Electron.*, vol. 8, no. 3, pp. 2716–2732, Sep. 2020.

[47] A. Rumi, J. G. Marinelli, P. Seri, M. Kohler, and A. Cavallini, "Performance of corona resistant insulation for aerospace," in *Proc. IEEE Electr. Insul. Conf. (EIC)*, Jun. 2021, pp. 22–25.

[48] H. Raether, *Electron Avalanches and Breakdown of Gases*, London, U.K.: Butterworths, 1964.

[49] X. Li, A. Sun, and J. Teunissen, "A computational study of negative surface discharges: Characteristics of surface streamers and surface charges," *IEEE Trans. Dielectr. Electr. Insul.*, vol. 27, no. 4, pp. 1178–1186, Aug. 2020.

[50] M. Florkowski, "Imaging and simulations of positive surface and airborne streamers adjacent to dielectric material," *Measurement*, vol. 186, Dec. 2021, Art. no. 110170.

[51] F. Manders, P. C. M. Christianen, and J. C. Maan, "Propagation of a streamer discharge in a magnetic field," *J. Phys. D, Appl. Phys.*, vol. 41, Nov. 2008, Art. no. 2340006.

[52] *COMSOL Multyphysics Users Guide 6.0*, Comsol AB, Sweden, 2020.

Marek Florkowski (Senior Member, IEEE) received the M.S. and Ph.D. degrees in electronics, and the Habilitation degree from the AGH University of Science and Technology, Kraków, Poland, in 1990, 1994, and 2009, respectively.

He is currently a Full Professor with the AGH University of Science and Technology. His research interests include diagnostics of electrical systems and devices, with a special focus on partial discharges mechanism, processing and analytics, high-voltage engineering, electronics and power electronics, energy conversion, signal and image processing, and advanced machine learning.

Dr. Florkowski is a member of CIGRE and the Polish Academy of Sciences. He is the Chair of the Technical Committee Diagnostics of the IEEE Dielectrics and Electrical Insulation Society and an Associate Editor of the IEEE TRANSACTIONS ON DIELECTRICS AND ELECTRICAL INSULATION.